N_2 AND CO DESORPTION ENERGIES FROM WATER ICE

Edith C. Fayolle, Jodi Balfe, Ryan Loomis, Jennifer Bergner, Dawn Graninger, Mahesh Rajappan, and Karin I. Öberg
Harvard-Smithsonian Center for Astrophysics, 60 Garden Street, Cambridge, MA 02138, USA

ABSTRACT

The relative desorption energies of CO and N_2 are key to interpretations of observed interstellar CO and N_2 abundance patterns, including the well-documented CO and N_2H^+ anti-correlations in disks, protostars, and molecular cloud cores. Based on laboratory experiments on pure CO and N_2 ice desorption, the difference between CO and N_2 desorption energies is small; the N_2-to-CO desorption energy ratio is 0.93 ± 0.03. Interstellar ices are not pure, however, and in this study we explore the effect of water ice on the desorption energy ratio of the two molecules. We present temperature programmed desorption experiments of different coverages of ^{13}CO and $^{15}N_2$ on porous and compact amorphous water ices and, for reference, of pure ices. In all experiments, $^{15}N_2$ desorption begins a few degrees before the onset of ^{13}CO desorption. The $^{15}N_2$ and ^{13}CO energy barriers are 770 and 866 K for the pure ices, 1034–1143 K and 1155–1298 K for different submonolayer coverages on compact water ice, and 1435 and 1575 K for ~1 ML of ice on top of porous water ice. For all equivalent experiments, the N_2-to-CO desorption energy ratio is consistently 0.9. Whenever CO and N_2 ice reside in similar ice environments (e.g., experience a similar degree of interaction with water ice) their desorption temperatures should thus be within a few degrees of one another. A smaller N_2-to-CO desorption energy ratio may be present in interstellar and circumstellar environments if the average CO ice molecules interacts more with water ice compared to the average N_2 molecules.

Key words: astrochemistry – ISM: abundances – ISM: molecules – methods: laboratory: solid state – molecular data – molecular processes

1. INTRODUCTION

The chemical structures of interstellar clouds, cloud cores, protostellar envelopes, and protoplanetary disks are all regulated by the differential freeze-out and desorption of the main carriers of oxygen, carbon, and nitrogen (Bergin & Langer 1997; Aikawa et al. 2002; Henning & Semenov 2013). The sequential freeze-out of atoms and molecules onto interstellar grains is the starting point for a rich surface chemistry that is, e.g., responsible for most of the water in space (van Dishoeck et al. 2013), as well as the abundant existence of complex, saturated molecules such as $HCOOCH_3$ (Garrod et al. 2008). Freeze-out also affects gas-phase compositions in multiple ways. For example, CO freeze-out is a prerequisite for abundant N_2H^+ in molecular clouds, protostars, and protoplanetary disks (Bergin et al. 2002; Jørgensen et al. 2005; Qi et al. 2013).

The balance of freeze-out and desorption in disks also affects several aspects of planet formation. Condensation fronts in the mid planes of protoplanetary disks, so-called snowlines, can enhance the planet formation efficiency due to increased grain surface density, rapid particle growth due to cold-head effects, pressure traps, and increased grain stickiness (Ciesla 2006; Johansen et al. 2007; Gundlach et al. 2011; Ros & Johansen 2013). Snowline locations also regulate the compositions of forming planets (Öberg et al. 2011a) and planetesimals. The locations of major snowlines depend on the volatile composition (e.g., whether most nitrogen is in N_2 or NH_3), a balance between freeze-out and thermal and non-thermal desorption rates at different disk locations, and disk dynamics (Öberg et al. 2011b; Oka et al. 2012; Ali-Dib et al. 2014; Baillié et al. 2015). Two of the most important volatiles in disks (as well as in clouds and protostars) are CO and N_2. Their desorption kinetics, fundamentally set by their binding energies, will determine the locations of two of the most important disk snowlines.

CO and N_2 binding energies have been the subject of several previous studies. In two related studies, Öberg et al. (2005) and Bisschop et al. (2006) found that the binding energies of CO and N_2 in pure, layered, and mixed $CO:N_2$ ices were relatively similar, i.e., the ratio of the N_2 to CO binding energies were 0.93–1. These experiments did not consider the effects of water. Experiments on CO deposited on water ice has shown that CO is substantially more strongly bound in water-dominated ices compared to pure CO ices (Noble et al. 2012); Collings et al. (2003a) found a 40% higher desorption energy for CO on top of low-density amorphous water ice compare to pure CO ice. There are no similarly detailed studies of N_2 interactions with water ice, but cluster calculations suggest that N_2 may not bind very strongly to water ice (Sadlej et al. 1995). Based on those calculations N_2 desorption energies of $0.65 \times E_{des}(CO)$ are sometimes used in astrochemical studies (e.g., Bergin & Langer 1997). Such a low N_2 binding energy compared to CO naturally explains the presence of N_2H^+ in cores and disks where CO has frozen out (e.g., Qi et al. 2013), but seems inconsistent with the experimentally measured small difference in binding energies of CO and N_2 in pure ices (Bisschop et al. 2006).

In this study we explore the effect of water on CO and N_2 desorption energies to astrophysically relevant ices. We aim to answer (i) whether the ratio of N_2 to CO binding energies in water-dominated ices deviate from the ratio of 0.93 found for pure ices, and (ii) whether the relative binding energies of CO and N_2 in water-dominated ices depend on the exact ice environment. In Section 2 we present the experimental method —temperature programmed desorption (TPD)—used to characterize CO and N_2 desorption. The experimental results and the derived CO and N_2 binding energies are presented in Section 3. The experimental results and their astrophysical implications are then discussed in Section 4.

2. METHODS

TPD experiments are used to derive the desorption energies of ^{13}CO or $^{15}N_2$ ices on CsI and H_2O substrates. Ices are grown by injecting molecules through a 4.8 mm diameter pipe at 0.7 inch from the substrate on a CsI window, resulting in a uniform ice. The window can be cooled to ~11 K using a close-cycle He cryostat, and is placed in an ultra-high vacuum chamber with base pressures of $<5.10^{-10}$ Torr at room temperature. More details on the experimental setup are given in Lauck et al. (2015). The vapor pressure of deionized water purified through at least three freeze–pump–thaw cycles using liquid nitrogen is deposited on the CsI window at (i) ~100 K to grow amorphous compact water ice substrates, and (ii) 11 K to grow amorphous porous water ice substrates. ^{13}CO (99% purity, Sigma-aldrich) and $^{15}N_2$ (98% purity, Sigma-aldrich) gases are then deposited at 11 K on top of the chosen substrate. The amount of molecules deposited is monitored during the injection using a calibrated quadrupole mass spectrometer (Pfeiffer QMG 220M1), integrating the mass spectrometer signal over time. The ice coverage is given in monolayer units with the typical approximation of 1 ML $= 10^{15}$ molecules cm^{-2}. The chamber is also equipped with a Fourier transform infrared spectrometer (Bruker Vertex 70v) in transmission mode to monitor the amount of infrared active molecules deposited on the window in the mid-infrared. ^{13}CO or $^{15}N_2$ ices of the desired thickness are then heated at a constant rate of 1 K minute^{-1}.

The temperature controller used to monitor the temperature is coupled to a thermocouple attached on a metallic window holder (Lakeshore 335). It has a relative uncertainty of 0.1 K but the absolute temperature is more difficult to assess since it depends on the thermal contact with the window holder it is attached to. We calibrated the temperature against initial CO TPD data obtained by the setup when the thermal contact was excellent (Cleeves et al. 2014), and for which the resulting CO desorption energy was within the average energy obtained in the literature (Collings et al. 2003a, 2015; Bisschop et al. 2006; Acharyya et al. 2007; Muñoz Caro et al. 2010; Martín-Doménech et al. 2014). We estimate that there is a 2 K absolute uncertainty on the temperature, based on the spread in the CO desorption energies found in the literature. The desorbing molecules are monitored using a quadrupole mass spectrometer (Hiden IDP 300, Model HAL 301 S/3) equipped with a pinhole on a translation stage that is approached 0.5 inches away from the CsI window. ^{13}CO and $^{15}N_2$ isotopologues ($m/z = 29$ and $m/z = 30$ respectively) are used to rule out possible contamination in the TPD results, due to background deposition of ^{12}CO and $^{14}N_2$ ($m/z = 28$ for both). Analysis of the TPD experiments showed that this contamination is minimal (lower than the purity percentage given by the manufacturer). The TPD plots in desorbing molecules per kelvin are obtained by subtracting the mass background for ^{13}CO or $^{15}N_2$ and scaling the QMS signal so the TPD integral over the temperature range is equal to the amount of molecules deposited. This assumes that the signal detected by the QMS is proportional to the amount of molecules desorbing and that the pumping speed in the chamber is high, both of which have been verified.

The experimental data set consists of various ^{13}CO or $^{15}N_2$ coverages deposited on the CsI window, on ~50 ML$_{eq}$ of compact amorphous water, and on ~50 ML$_{eq}$ of porous amorphous water. The TPD curves are fit using the Polanyi–Wigner equation:

$$-\frac{d\theta}{dT} = \frac{\nu}{\beta} \theta^n e^{-E_{des}/T}, \quad (1)$$

where θ is the ice coverage, T the temperature in K, ν a pre-exponential factor in s^{-1}, β the heating rate in K s^{-1}, n the desorption order, and E_{des} the desorption energy in K. To derive the desorption energies, we describe the desorption kinetics using two different regimes: a multilayer regime regulated by ^{13}CO–^{13}CO or $^{15}N_2$–$^{15}N_2$ binding energies, resulting in a zeroth-order kinetics ($n = 0$ in Equation (1)) and a submonolayer regime where ^{13}CO or $^{15}N_2$ are in contact with the substrate, resulting in a first-order desorption. The zeroth-order regime is usually well fit by only one single desorption energy and the submonolayer regime needs to be described using a distribution of desorption energies. This is due to the different adsorption sites from a disordered and rough substrate, as reported recently by Noble et al. (2012), Collings et al. (2015), and Doronin et al. (2015), using models based on work by Redhead (1962), Koch et al. (1997), and Tait et al. (2005). For the pre-exponential factor associated with ^{13}CO and $^{15}N_2$, we use the harmonic oscillator relation (e.g., Hasegawa et al. 1992; Acharyya et al. 2007; Noble et al. 2012):

$$\nu = \sqrt{\frac{2 n_s E_{des}}{\pi^2 m}}, \quad (2)$$

where n_s is the number of adsorption sites (~10^{19} sites.m^{-2}) and m is the mass of the molecule in kg. This approximation is valid in the case of small molecules like CO and N_2, but is not appropriate for large molecules, since it relies on internal and translational degrees of freedom being equivalent for the adsorbed and desorbing molecule (e.g., Müller et al. 2003). The value of the pre-exponential factor affects the derived desorption energy values, but not the ratio of CO and N_2 desorption energies, even when the factor is varied over many orders of magnitude.

3. RESULTS

The TPD curves of ^{13}CO or $^{15}N_2$ on the CsI substrate, compact, and porous amorphous water are shown in Figure 1. In the top panel, ~5 ML of ^{13}CO or $^{15}N_2$ are deposited on the CsI window, then warmed up at 1 K minute^{-1}. The desorption peaks at temperatures of 24.9 K for $^{15}N_2$ and 28.2 K for ^{13}CO. The shape of the curve is similar to a zeroth-order desorption with an irregular desorption tail, indicative of different submonolayer binding site on the CsI window and perhaps also the window holder. The middle panel of Figure 1 shows the TPD curves of ~0.7 ML of ^{13}CO or $^{15}N_2$ deposited on an amorphous compact thick water ice (~50 ML) and warmed up at 1 K minute^{-1}. The curve has two peaks, which can be attributed to desorption from pure ice and desorption from the water substrate. The second peak, associated with the submonolayer interaction of the diatomic species with H_2O, is much broader than the desorption in the multilayer regime and peaks at 32.4 K for $^{15}N_2$ and at 36.6 K for ^{13}CO. The bottom panel shows the TPD curves of 2 ML of ^{13}CO or $^{15}N_2$ deposited on amorphous porous water. From the porous H_2O ice ($T_{deposition} = 11$ K), ^{13}CO and $^{15}N_2$ present two desorption peaks, one at 43 and 47 K, respectively, and one close to the
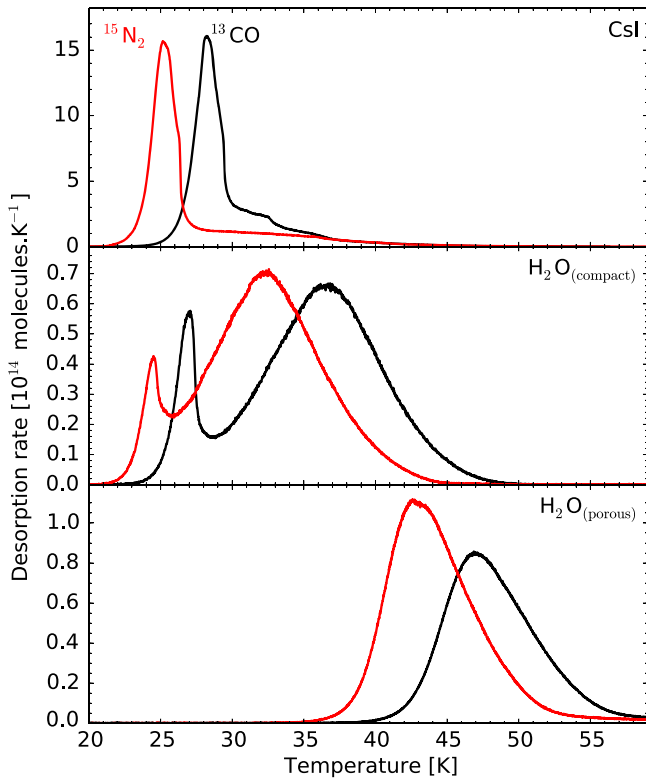
Figure 1. ^{13}CO (solid black lines) and $^{15}N_2$ (solid red lines) TPD curves from pure ice and H_2O ice surface at 1 K minute^{-1}. The upper panel presents the desorption of 5 ML of ^{13}CO and 5 ML of $^{15}N_2$ deposited on a CsI window. The middle panel shows the desorption of 0.8 ML of ^{13}CO and 0.7 ML of $^{15}N_2$ deposited on amorphous compact water (grown at 100 K). The lower panel shows the TPD curves of 2 ML ^{13}CO and 2 ML of $^{15}N_2$ up to 65 K deposited on amorphous porous water (previously deposited at 14 K). For these later experiments, only 0.7 ML of ^{13}CO and 0.8 ML of $^{15}N_2$ desorb below 65 K since a fraction of ^{13}CO or $^{15}N_2$ stays trapped within the H_2O ice.

water desorption temperature due to release of entrapped molecules (not shown here). This latter feature is due to volatile entrapment within the ice pores (e.g., Collings et al. 2003b; Bar-Nun et al. 2007; Fayolle et al. 2011; Martín-Doménech et al. 2014). 0.7 ML–0.8 ML of ^{13}CO and $^{15}N_2$ desorbed below 65 K while the rest was entrapped with H_2O.

The experiments described above clearly demonstrate that $^{15}N_2$ desorption behavior is strongly affected by the presence of water, similarly to what has previously been observed for CO. The temperature shifts between pure ice desorption from compact and porous amorphous water ice appear to be similar for the two molecules.

To better comprehend the effect of the water substrate on ^{13}CO and $^{15}N_2$ desorption kinetics, we performed a series of TPD experiments for different coverages on amorphous compact water. The results are shown in the left panels of Figure 2. For high coverages above 0.7 ML, both a multilayer and a submonolayer component are present in the TPD curves. Note that the presence of a multilayer component below one monolayer could either be due to a lower surface site density than the assumed value of 10^{15} molecules cm^{-2} or to a non-uniform wetting of the surface resulting in the formation of islands. For lower coverages, only the submonolayer desorption peak is present. For both ^{13}CO and $^{15}N_2$, the submonolayer peak shifts toward higher temperatures with decreasing coverage. This coverage trend on compact

amorphous water was also observed by Noble et al. (2012) for CO, who explained it by CO adsorbing first to the strongest bounding sites on the water substrate.

To quantify the desorption energy of these systems, we fit the TPD curves using the Polanyi–Wigner equation (Equation (1) in Section 2), assuming zeroth order for the 5 ML experiments on bare CsI window. We fit the logarithm of the desorbing molecules versus the inverse of the temperature with a straight line (e.g., Doronin et al. 2015), yielding desorption energies for pure ices of 770 ± 68 K for $^{15}N_2$ and 866 ± 68 K for ^{13}CO (Table 1, first row). The associated error mainly comes from the absolute uncertainty on the temperature while the relative uncertainty on the fit is less than 5 K. These desorption energy values result in pre-exponential factor values of 6.5×10^{11} s^{-1} for $^{15}N_2$ and 7.1×10^{11} s^{-1} for ^{13}CO using Equation (2). Note that an empirical determination of the pre-exponential factor, using the intercept of the straight line fitting explained above, yields values of 6.6×10^{11} s^{-1} for $^{15}N_2$ and 8.0×10^{11} s^{-1} for ^{13}CO, which are in good agreement with the theoretical values. The desorption energies are consistent with literature data from Öberg et al. (2005) of 790 ± 25 K and 855 ± 25 K for N_2 and CO, from Noble et al. (2012) of 828 ± 28 K for CO, and CO desorption energies from Collings et al. (2015) of 830 ± 36 K. Our N_2 desorption energy is substantially lower, however, than their measured value of 878 ± 36 K.

To derive desorption energies for the submonolayer regime, we used a distribution of binding energies obtained by fitting the submonolayer regime of the TPD curves by a linear combination of first-order kinetics, sampling the desorption energy by steps of 30 K between 670 and 1650 K. This technique takes into account the non-homogeneous nature of the amorphous water ice surface and has been recently used by Doronin et al. (2015) in the case of methanol adsorbed on graphite. The fitting is done in python using *scipy.optimize. nnls*, a non-negative least-squares fitting module, so the linear combination coefficients are kept positive. The linear combination coefficients are normalized to the initial coverages, yielding fractional coverages, and are plotted in the right panels of Figure 2 versus the sampled desorption energy. The data are smoothed using a Gaussian filter and plotted in dashed lines for clarity as well. All the distributions are close to symmetric around the mean and present FWHMs of 113–139 K, resulting in well-defined "representative" desorption energies for each coverage. The mean energy is known with a ∼30 K relative precision due to the chosen sampling energy steps (the uncertainty from the fit is smaller), and has an absolute uncertainty of 67 K. As noted for the TPD curves, the desorption distribution and their trends for various coverages are similar for ^{13}CO and $^{15}N_2$. The mean desorption energy values and the FWHM are reported in Table 1. The mean submonolayer desorption energy from a compact water ice surface ranges from 1034 to 1143 K for $^{15}N_2$ and 1155 to 1575 K for ^{13}CO. The shift toward higher energy for decreasing submonolayer coverages is consistent with data from Noble et al. (2012) for CO on amorphous compact water. The resulting pre-exponential factor values from Equation (2) are between 6 and 10×10^{11} s^{-1} over the sampled desorption energy range.

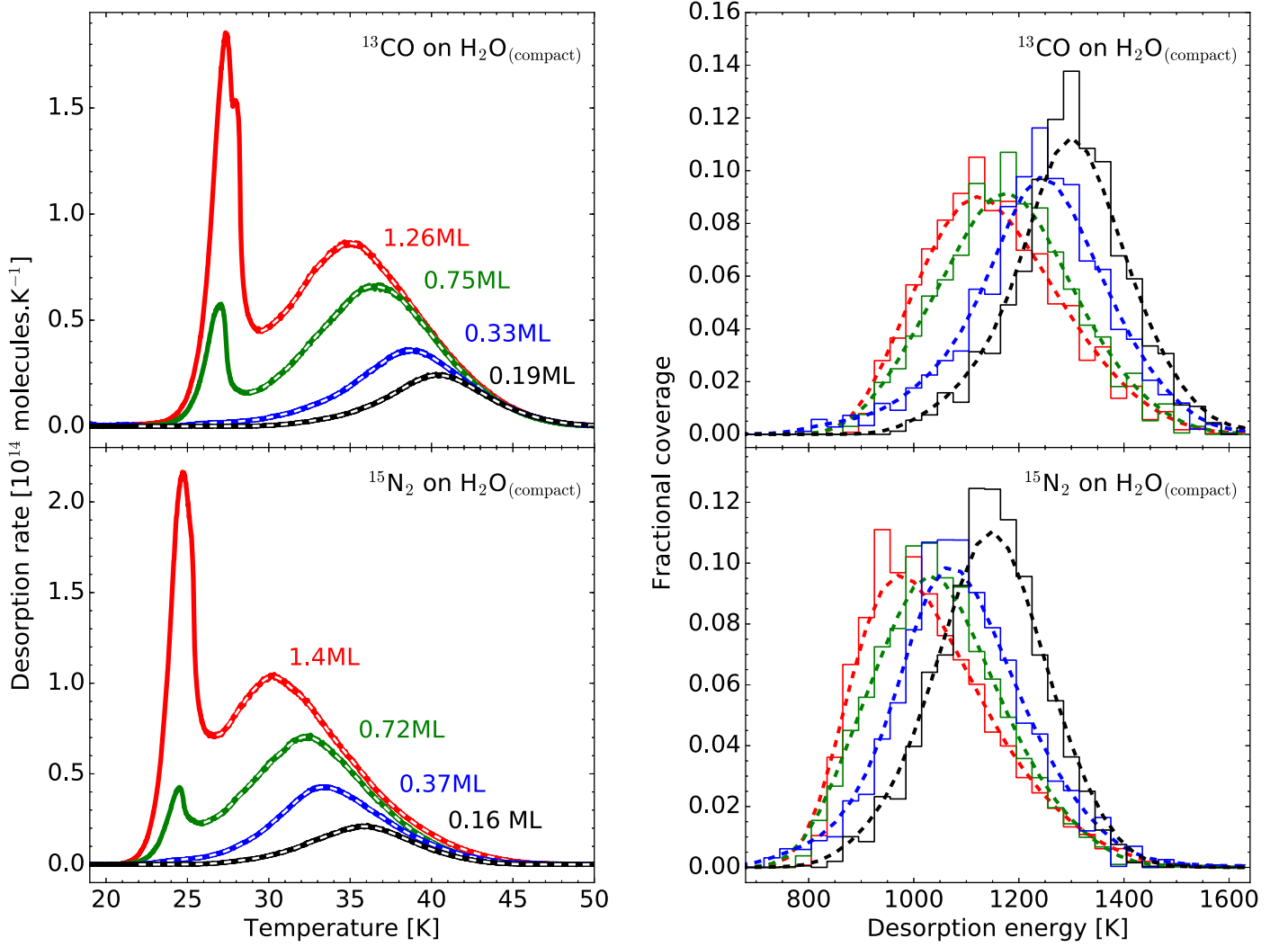The desorption energies obtained for all the $^{15}N_2$ experiments are plotted versus those of ^{13}CO in Figure 3.

Figure 2. ^{13}CO (left upper panel) and $^{15}N_2$ (left bottom panel) temperature desorption curves for various coverages on amorphous compact H_2O and the corresponding desorption energy distribution for ^{13}CO (right upper panel) and $^{15}N_2$ (right bottom panel). On the left panel, the TPD data are the solid lines while the white dashed lines show the fit obtained with the corresponding energy distribution. In the right panel, the histograms show the fitted fractional coverage associated to a desorption energy and the dashed lines are the smoothed distribution using a Gaussian filter for clarity.

Table 1
Coverages, Desorption Energy for the Pure Ice Multilayer Regime or Mean Desorption Energy with FWHM for the Submonolayer Regime on Water Substrate, and the $^{15}N_2$ to ^{13}CO Desorption Energy Ratio for Various Substrates

Substrate	^{13}CO		$^{15}N_2$		$E_{des}\ ^{15}N_2 / E_{des}\ ^{13}CO$
	Coverage/ML	E_{des}/K	Coverage/ML	E_{des}/K	
Pure ice	5.0	866 ± 68[a]	5.3	770 ± 68[a]	0.89 ± 0.02
H_2O (compact)	1.3	1155 [133]	1.4	1034 [133]	0.90 ± 0.04
H_2O (compact)	0.8	1180 [131]	0.7	1051 [127]	0.89 ± 0.04
H_2O (compact)	0.3	1236 [139]	0.4	1090 [133]	0.88 ± 0.04
H_2O (compact)	0.2	1298 [116]	0.2	1143 [113]	0.88 ± 0.04
H_2O (porous)	0.7	1575 [117]	0.8	1435 [132]	0.91 ± 0.03

Note.
[a] The pure ice desorption energies are obtained by a zeroth-order fit and are given with uncertainties mainly due to the absolute error on the temperature.

The data is consistent with a single ratio of ∼0.9 and inconsistent with a ratio of 0.65. The desorption energy ratio of $^{15}N_2$ over ^{13}CO for the multilayer (pure ice) and the mean desorption energy ratio of $^{15}N_2$ over ^{13}CO for the submonolayer coverages are also listed in Table 1; the values span 0.88–0.91.

4. ASTROPHYSICAL IMPLICATIONS

The locations of condensation fronts (snowlines) in disks, protostars and clouds depend on the desorption energies of the volatiles in question. These desorption energies increase dramatically when CO or N_2 desorbs from water ice. The highest desorption energies barriers of ∼1610 and 1470 K for
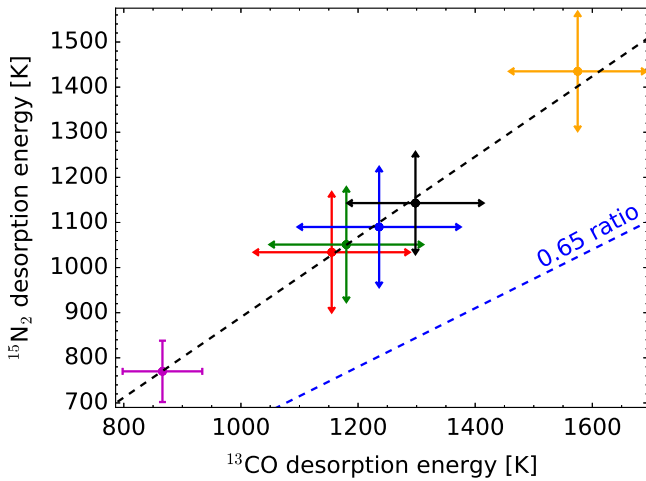
Figure 3. $^{15}N_2$ vs. ^{13}CO desorption energies and associated error bar for the pure ice multilayer regime (magenta symbols) and mean desorption energies for the submonolayer regimes on water substrates (red, green, blue, and black for the 1.4–1.3 ML, 0.7–0.8 ML, 0.4–0.3 ML, and 0.2 ML coverages on amorphous compact water, and orange symbol for $^{15}N_2$ and ^{13}CO deposited on amorphous porous water). The black dashed line represents the fitted ratio of 0.89 and the blue dashed line shows the 0.65 ratio assumed in some astrochemical models to explain the observed CO and N_2H^+ abundances (Bergin & Langer 1997).

CO and N_2, respectively, are achieved when CO and N_2 are deposited on a porous water ice surface where each CO or N_2 molecules can interact with multiple H_2O molecules. The large effects of water ice on the CO desorption energy was known from previous experiments (Collings et al. 2003b; Noble et al. 2012). Our study shows that N_2 is similarly affected, and both molecules are therefore likely to present ranges of thermal desorption temperatures in different interstellar and circumstellar environments. In a typical protoplanetary disk a change in desorption energy from 770 to 1435 K results in a change in N_2 snowline location from ~50 to ~20 AU. This estimate is based on the median temperature disk profile $T = 200 K \times (r/1 AU)^{-0.62}$ from Andrews & Williams (2007) and using the prescription from Hollenbach et al. (2009) to calculate the sublimation temperatures from the desorption energies. In the Solar Nebula this difference in N_2 snowline location between 50 and 20 AU is the difference between comets and the Ice Giants forming nitrogen rich or nitrogen poor (Tsiganis et al. 2005).

The second astrophysically important result of our experiments is the similarity of the N_2 and CO desorption kinetics and energies in different ice environments. Whether the ices are pure or deposited on top of different kinds of amorphous water ices, and whether the ices are more than a monolayer thick or a fraction of a monolayer, the ratio between the N_2 and CO desorption energies is consistently 0.9. This implies that in astrophysical environments where CO and N_2 ices experience similar levels of interaction with water ice, the N_2 desorption energy and temperature can always be parameterized as a fraction (0.9) of the CO desorption energy and temperature.

While the N_2-to-CO desorption energy ratio is certainly not unity, it is not close to the value of 0.65 preferred in some observational studies. In cloud cores, different formation kinetics of CO and N_2 in the gas phase may be sufficient to explain the later freeze-out of N_2, but in disks, where high densities result in short chemical timescales it is less clear that a

N_2-to-CO desorption energy ratio of 0.9 is sufficient to explain observed N_2H^+ emission exterior to the CO snowline.

It is plausible, however, that N_2 on average is interacting with a less H_2O-rich environment than CO. Garrod & Pauly (2011) finds that the H_2O abundance in ices decreases with increasing ice coverage when modeling ice formation in dark clouds, i.e., the number of H_2O molecules in a specific ice layer is less in the upper layers of the ice mantle that formed at a later time compared to the lower layers of the ice mantle. There are two reasons why N_2 ice may form slightly later than CO ice and thus be mainly present in the top-most, water-poor ice layers. First, the N_2 desorption temperature is slightly lower, which may be sufficient to keep N_2 in the gas phase at lower temperature than CO if the freeze-out timescales are long enough. Second, the nitrogen chemistry is slower compared to the CO one, which may cause N_2 ice to preferentially form later than CO ice (Hily-Blant et al. 2010; Pagani et al. 2012). Both effects could contribute to the observed CO and N_2H^+ anti-correlation in molecular cloud cores. In disks, where the gas-phase chemistry is expected to reach steady state quickly, the different gas-phase timescales of N_2 and CO are not expected to play a role, but a slight differential freeze-out could. Differential freeze-out of CO and N_2 may also result in a high non-thermal desorption efficiency of N_2 compared to CO. Bertin et al. (2013) found that N_2 ice UV photodesorption is very efficient and CO photodesorption is quenched if a CO ice is covered by a few N_2 ice layers.

In summary, both CO and N_2 ice thermal desorption depend strongly on the ice morphology and composition. Based on our experiments, N_2 and CO desorption energies are substantially elevated, when molecules are desorbing from an amorphous water ice surface compared to a pure ice. As long as this morphology and composition are equivalent for the two molecules, the N_2 desorption energy is 0.9 that of the CO desorption energy. Differential freeze-out may increase the difference, but detailed modeling is required to assess the feasibility of this scenario.

REFERENCES

Acharyya, K., Fuchs, G. W., Fraser, H. J., van Dishoeck, E. F., & Linnartz, H. 2007, A&A, 466, 1005
Aikawa, Y., van Zadelhoff, G. J., van Dishoeck, E. F., & Herbst, E. 2002, A&A, 386, 622
Ali-Dib, M., Mousis, O., Petit, J.-M., & Lunine, J. I. 2014, ApJ, 793, 9
Andrews, S. M., & Williams, J. P. 2007, ApJ, 659, 705
Baillié, K., Charnoz, S., & Pantin, E. 2015, A&A, 577, A65
Bar-Nun, A., Notesco, G., & Owen, T. 2007, Icar, 190, 655
Bergin, E. A., Alves, J., Huard, T., & Lada, C. J. 2002, ApJL, 570, L101
Bergin, E. A., & Langer, W. D. 1997, ApJ, 486, 316
Bertin, M., Fayolle, E. C., Romanzin, C., et al. 2013, ApJ, 779, 120
Bisschop, S. E., Fraser, H. J., Öberg, K. I., van Dishoeck, E. F., & Schlemmer, S. 2006, A&A, 449, 1297
Ciesla, F. J. 2006, ApJL, 654, L159
Cleeves, L. I., Bergin, E. A., Alexander, C. M. O., et al. 2014, Sci, 345, 1590
Collings, M. P., Dever, J. W., Fraser, H. J., & McCoustra, M. R. S. 2003a, Ap&SS, 285, 633
Collings, M. P., Dever, J. W., Fraser, H. J., McCoustra, M. R. S., & Williams, D. A. 2003b, ApJ, 583, 1058

Collings, M. P., Frankland, V. L., Lasne, J., et al. 2015, MNRAS, 449, 1826

Doronin, M., Bertin, M., Michaut, X., Philippe, L., & Fillion, J.-H. 2015, JChPh, 143, 084703

Fayolle, E. C., Öberg, K. I., Cuppen, H. M., Visser, R., & Linnartz, H. 2011, A&A, 529, A74

Garrod, R. T., & Pauly, T. 2011, ApJ, 735, 15

Garrod, R. T., Weaver, S. L. W., & Herbst, E. 2008, ApJ, 682, 283

Gundlach, B., Kilias, S., Beitz, E., & Blum, J. 2011, Icar, 214, 717

Hasegawa, T. I., Herbst, E., & Leung, C. M. 1992, ApJS, 82, 167

Henning, T., & Semenov, D. 2013, ChRv, 113, 9016

Hily-Blant, P., Walmsley, M., Pineau Des Forêts, G., & Flower, D. 2010, A&A, 513, A41

Hollenbach, D., Kaufman, M. J., Bergin, E. A., & Melnick, G. J. 2009, ApJ, 690, 1497

Johansen, A., Oishi, J. S., Mac Low, M.-M., et al. 2007, Natur, 448, 1022

Jørgensen, J. K., Schöier, F. L., & van Dishoeck, E. F. 2005, A&A, 435, 177

Koch, K., Hunger, B., Klepel, O., & Heuchel, M. 1997, Journal of Catalysis, 172, 187

Lauck, T., Karssemeijer, L., Shulenberger, K., et al. 2015, ApJ, 801, 118

Martín-Doménech, R., Muñoz Caro, G. M., Bueno, J., & Goesmann, F. 2014, A&A, 564, A8

Müller, T., Flynn, G. W., Mathauser, A. T., & Teplyakov, A. V. 2003, Langm, 19, 2812

Muñoz Caro, G. M., Jiménez-Escobar, A., Martín-Gago, J. Á., et al. 2010, A&A, 522, A108

Noble, J. A., Congiu, E., Dulieu, F., & Fraser, H. J. 2012, MNRAS, 421, 768

Öberg, K. I., Murray-Clay, R., & Bergin, E. A. 2011a, ApJL, 743, L16

Öberg, K. I., Qi, C., Fogel, J. K. J., et al. 2011b, ApJ, 734, 98

Öberg, K. I., van Broekhuizen, F., Fraser, H. J., et al. 2005, ApJL, 621, L33

Oka, A., Inoue, A. K., Nakamoto, T., & Honda, M. 2012, ApJ, 747, 138

Pagani, L., Bourgoin, A., & Lique, F. 2012, A&A, 548, L4

Qi, C., Öberg, K. I., & Wilner, D. J. 2013, ApJ, 765, 34

Redhead, P. A. 1962, Vacuu, 12, 203

Ros, K., & Johansen, A. 2013, A&A, 552, A137

Sadlej, J., Rowland, B., Devlin, J. P., & Buch, V. 1995, JChPh, 102, 4804

Tait, S. L., Dohnálek, Z., Campbell, C. T., & Kay, B. D. 2005, JChPh, 122, 164707

Tsiganis, K., Gomes, R., Morbidelli, A., & Levison, H. F. 2005, Natur, 435, 459

van Dishoeck, E. F., Herbst, E., & Neufeld, D. A. 2013, ChRv, 113, 9043